The Journal of Supercritical Fluids 188 (2022) 105692

Contents lists available at ScienceDirect

The Journal of Supercritical Fluids

journal homepage: www.elsevier.com/locate/supflu

Formation and evolution characteristics of hydrothermal flames inside a transpiring wall reactor: A transient numerical investigation

Zhaojian Liang [a,b], Fengming Zhang [a,c,*], Mengying Li [b], Chunyuan Ma [d]

[a] Guangzhou Institute of Advanced Technology, Guangzhou, China
[b] Department of Mechanical Engineering & Research Institute for Smart Energy, The Hong Kong Polytechnic University, Hung Hom, Hong Kong Special Administrative Region
[c] Shenzhen Institute of Advanced Technology, Chinese Academy of Sciences, Shenzhen, China
[d] National Engineering Laboratory for Coal-fired Pollutants Emission Reduction, Shandong University, Jinan, Shandong Province, China

ARTICLE INFO

Keywords:
Hydrothermal flame
Transpiring wall reactor
Supercritical water oxidation
Transient simulation
Negative buoyant jet

ABSTRACT

Transpiring-wall reactors with hydrothermal flames are effective in preventing corrosion and salt deposition in supercritical water oxidation systems. To uncover the not-well-understood evolution characteristics of the hydrothermal flame surrounded by a transpiring water film, a 2-D unsteady simulation is firstly conducted in this study. The transient results show that the variations of flow fields and flame shapes are attributed to the competition between inertial forces and buoyant forces. And the quasi-steady results present that high feed concentration may damage transpiring wall and delay the evolution of hydrothermal flames. In addition, a low feed temperature or a big flow area of jet can lead to open hydrothermal flames, which adversely affect the reactor. Furthermore, Froude Number, Fr, shows effectiveness in predicting quasi-steady flame shapes. For large-Fr conditions, the inertial force outweighs the buoyant force and hence closed flames are developed; while for low-Fr cases, open flames are developed.

1. Introduction

The supercritical water oxidation (SCWO) system is an efficient approach to degrade organics in wastewater. SCWO denotes oxidations that are carried out in supercritical water (SCW). At supercritical state (P > 22.1 MPa, T > 374.3 °C), the liquid–gas interface disappears [1]; water behaves as a non-polar solvent, which is completely miscible with non-polar organic compounds and gases such as O_2, CO_2, and N_2 [2]. Thus, the SCWO system is a homogeneous reaction system that only involves a single fluid phase without any interfacial mass transport limitations among organic compounds, oxygen, and SCW [3]. The main problems that hinder the commercialization of SCWO are corrosion and salt deposition [4]. The transpiring-wall reactor (TWR) is a promising solution to these problems. In the TWR, an outer vessel is used to resist pressure, and a coaxial inner porous tube is used to resist high temperature and corrosive substances. Transpiring water (TW) is injected from the outer vessel radially to form a water film on the porous inner tube. The water film can dilute corrosive salts and cool down nearby high-temperature stream [5]. However, unexpected salt precipitating and coking will occur in the preheating section of the TWR when high temperature (400 °C to 550 °C) is required to preheat the feed [6]. The fouling generated in the preheating section is harmful to heat exchangers and electrical heaters, and may lead to logging and shut-down of the system.

The introduction of a hydrothermal flame to the TWR is an effective solution to solve the preheating problems and enhance the feed degradation [7,8]. The hydrothermal flame, which is defined as the flame produced in the SCW [9], behaves as an internal heat source that allows the feed to be preheated inside of the reactor, and hence avoids the coking and plugging issues in the preheating section. In terms of the feed degradation, the hydrothermal flames take place at a higher temperature (650 °C to 1200 °C) in comparison to the mild reaction temperature (400 °C to 600 °C) for the tradition SCWO and thus require shorter residence time (10 ms to 100 ms) to achieve complete degradation of organics matters [9]. Therefore, the TWR containing the hydrothermal flame shows high industrial value in the organic wastewater treatment, especially for wastewater with high salinity or high solid content.

Ignition and extinction are critical to the safe and reliable operation of the hydrothermal flame [11–13]. However, experimental measuring and imaging of the hydrothermal flame are very difficult because of the harsh reaction environment. Therefore, only a few relevant experiments have been conducted in the literature. Wellig et al. [14]

* Corresponding author at: Guangzhou Institute of Advanced Technology, Guangzhou, China.
E-mail address: fm.zhang@giat.ac.cn (F. Zhang).

https://doi.org/10.1016/j.supflu.2022.105692
Received 21 March 2022; Received in revised form 13 July 2022; Accepted 15 July 2022
Available online 18 July 2022

Nomenclature

Symbols

$1/\alpha$	Viscous coefficient, 2.5×10^{11} in axial direction, 2.5×10^{14} in radial direction, [$1/m^2$]
β	Inertial coefficient, 9×10^5 in axial direction, 9×10^8 in radial direction, [1/m]
χ	Porosity of the medium, 0.4
δ_{ij}	Kronecker Delta
$\dot{H}$	Enthalpy flow rate, [J/s]
$\dot{m}$	Mass flow rate, [kg/s]
λ	Thermal conductivity, [W/m K]
μ	Molecular viscosity, [kg/m s]
μ_t	Turbulent viscosity, [kg/m s]
ω	Mass fraction
ρ	Density, [kg/m^3]
Pr_t	Turbulent Prandtl number, 0.85
Sc_t	Turbulent Schmidt number, 0.7
σ_ε	Turbulent Prandtl numbers for ε
σ_k	Turbulent Prandtl numbers for k
ε	Turbulent dissipation rate, [m^2/s^3]
C_μ	A variable in Realizable $k-\varepsilon$ model, which is computed based on the mean strain and rotation rates, the angular velocity of the system rotation, and the turbulent dissipation rate
c_P	Specific heat, [J/kg K]
D_m	Mass diffusivity, [m^2/s]
D_T	Thermal diffusion coefficient, [m^2/s]
E	Total energy, [J/kg]
g	Gravitational constant, [m/s^2]
G_b	Generation term of k due to buoyancy, [W/m^3]
h	Specific sensible enthalpy, [J/kg]
h_c^0	heat of combustion of CH_3OH, [J/kg]
I	Unity tensor
k	Turbulent kinetic energy, [J/kg]
L	Characteristic length, [m]
p	Static pressure, [Pa]
R	Radial distance, [m]
S_R	Net rate of production due to chemical reaction, [kg/m^3 s]
T	Temperature, [K]
t	Time, [s]
u	Velocity, [m/s]
W_{AJI}	Width of the annular nozzle, [m]
X	Axial distance, [m]
y^+	Non-dimensional wall distance
Y_M	Contribution of fluctuating dilatation in compressible turbulence to overall dissipation rate, [W/m^3]
G_k	Generation term of k due to mean velocity gradients, [W/m^3]
Fr	Froude Number

Subscripts

$\mathcal{R}$	Reactants
n	Species n
eff.	Effective
f	Fluid
noz	Nozzle
s	Solid
top	Top region

Abbreviations

AJI	Annular-jet inlet
CJI	Central-jet inlet
CV	Control volume
EWT	Enhanced Wall Treatment
OER	Oxygen excess ratio
SCW	Supercritical water
SCWO	Supercritical water oxidation
TW	Transpiring water
TWR	Transpiring-wall reactor
URANS	Unsteady Reynolds-averaged Navier–Stokes

investigated extinction characteristics of methanol solution in the TWR. The results indicated that the extinction temperature sharply decreases with increasing feed concentration. Bermejo et al. [15] and Zhang et al. [16] reported the effectiveness of nozzle structure optimization in reducing the extinction temperature. Cabeza et al. [17] pointed out the prerequisite for the hydrothermal flame formation in a tubular reactor, which is the supercritical temperature of feed, and good stability of the hydrothermal flame in a vessel reactor due to back mixing effect. In comparison to measurement, the direct observation of the hydrothermal flame is more expensive, which generally requires a sapphire window and a high-speed camera. Serikawa et al. [18] obtained images of the isopropanol hydrothermal flame from ignition to extinction and acquired concentration conditions for hydrothermal flame formation. Sobhy et al. [19] used methanol and air to generate a laminar reverse diffusion flame and studied the influence of hydrothermal flame on the formation of nitrogen oxides (NO_x). Hicks et al. [20] found that ignition generally occurred in downstream where ethanol and air were fully mixed, and the flame gradually intensified after stabilizing from the burner outlet.

Due to the limitations of experimental methods, numerical simulation becomes an indispensable tool to study flames at supercritical state [21–23]. To date, some studies analyzed the characteristics and mechanisms of hydrothermal flames. Ren et al. [24,25] established a detailed chemical kinetic model of methanol and investigated effects of turbulence on structures of the hydrothermal flame. Song et al. [26] conducted a direct numerical simulation on the auto-ignition process in the non-premixed hydrothermal flames and reported the lack of rich premixed branches in the hydrothermal flame. The same authors in another study [27] found that the hydrothermal flame is mainly stabilized by spontaneous combustions. The authors also claimed that the contribution of flame propagation to flame stability increases with time and oxidant temperature. Reddy et al. [28] indicated that the inertia force and the buoyant force under high velocity can reduce ignition delay of the hydrothermal flame.

Whereas, studies on the hydrothermal flame in the TWR are rarely found in the literature. Via experiments, Zhang et al. [29] indicated that interactions between the hydrothermal flame and TW greatly affect the feed degradation and stability of the hydrothermal flame in the TWR system. Two numerical studies [30,31] revealed the complex heat and mass transfer phenomena induced by the interactions between radial TW and axial reactive fluids. However, the previous numerical studies only focused on steady state conditions and neglected gravity. Thus, there is a lack of numerical investigations on the transient

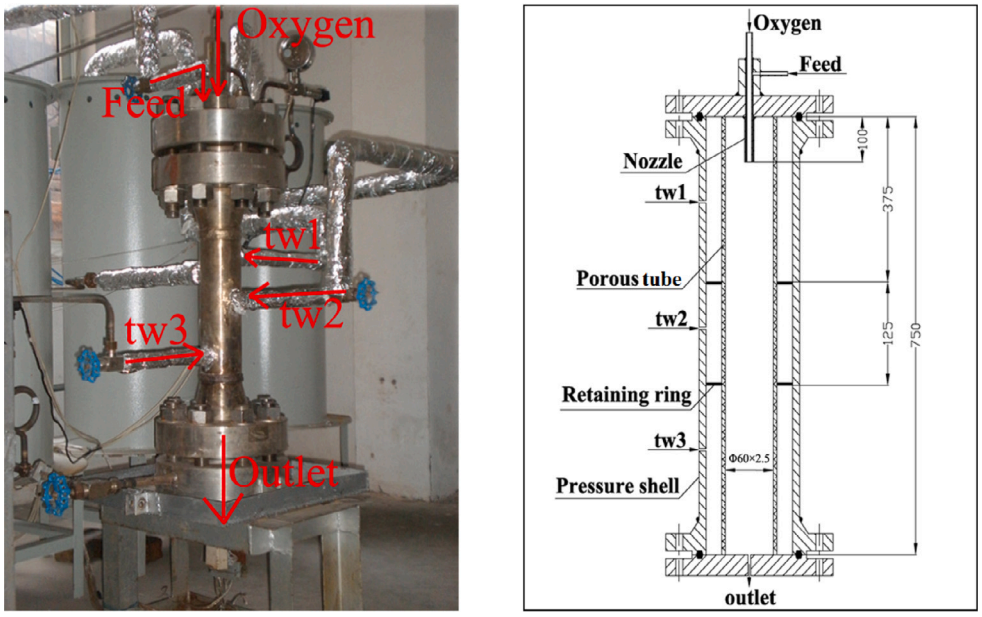

(a) Exterior of test rig. (b) Interior diagram of test rig.

Fig. 1. Experimental rig of TWR [10].

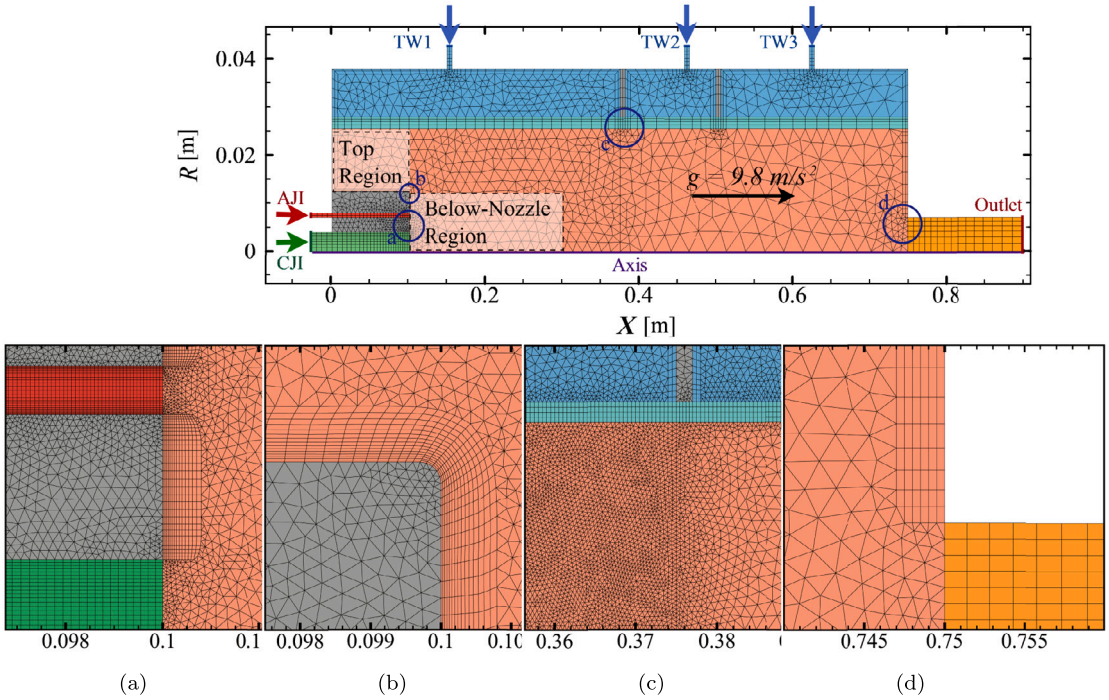

Fig. 2. Illustration of model geometry and real-size meshes. Colored regions include annular jet (■), central jet (■), transpiring-water region (■), reaction region (■), porous media (■), outlet channel (■), and solid (■). Marked boundaries include five inlets — annular jet inlet (AJI), central jet inlet (CJI), transpiring water inlet 1 (TW1), TW2, and TW3, one outlet, and central (symmetrical) axis. Unmarked boundaries are reactor walls.

formation and evolution characteristics of the hydrothermal flames in the TWR. To fill the research gap, a transient numerical simulation is firstly conducted on the hydrothermal flames inside an TWR in this work. Details and limitations of the numerical model are presented in Section 2; formation and evolution characteristics of the hydrothermal flame are investigated in Section 3.1; effects of nozzle structure, feed temperature, and feed concentration on the flame shape are evaluated in Sections 3.2 and 3.3. Conclusions are summarized in Section 4.

2. Numerical method

2.1. Model geometry

The experimental set-up and the structure diagram of the investigated TWR are shown in Fig. 1. The reactor mainly consists of a concentric nozzle, a porous tube, two retaining rings, a pressure shell, and three TW inlets. Oxygen and the feed are injected into the

Table 1
Summary of governing equations [32].

Governing equations of fluids	
Continuity	$\frac{\partial \rho}{\partial t} + \frac{\partial}{\partial x_i}\left(\rho u_i\right) = 0$
Momentum	$\frac{\partial}{\partial t}\left(\rho u_i\right) + \frac{\partial}{\partial x_j}\left(\rho u_i u_j\right) =$ $-\frac{\partial p}{\partial x_i} + \frac{\partial}{\partial x_j}\left[\mu\left(\frac{\partial u_i}{\partial x_j} + \frac{\partial u_j}{\partial x_i} - \frac{2}{3}\delta_{ij}\frac{\partial u_i}{\partial x_i}\right)\right] + \frac{\partial}{\partial x_j}\left(-\rho\overline{u_i' u_j'}\right) + \rho g_i + f_i$ $-\rho\overline{u_i' u_j'} = \mu_t\left(\frac{\partial u_i}{\partial x_j} + \frac{\partial u_j}{\partial x_i}\right) - \frac{2}{3}\left(\rho k + \mu_t\frac{\partial u_k}{\partial x_k}\right)\delta_{ij}, f_i = 0$
Energy	$\frac{\partial}{\partial t}(\rho E) + \frac{\partial}{\partial x_i}\left[u_i(\rho E + p)\right] = \frac{\partial}{\partial x_j}\left[\left(\lambda + \frac{c_p \mu_t}{\mathrm{Pr}_t}\right)\frac{\partial T}{\partial x_j} - \left(\sum_n h_n J_{jn}\right) + u_i\left(\tau_{ij}\right)_{\mathrm{eff.}}\right]$ $E = h - \frac{p}{\rho} + \frac{\lvert u\rvert^2}{2},\ h = \int_{298.15\mathrm{K}}^{T} c_P dT,$ $\left(\tau_{ij}\right)_{\mathrm{eff.}} = \mu_{\mathrm{eff.}}\left(\frac{\partial u_j}{\partial x_i} + \frac{\partial u_i}{\partial x_j}\right) - \frac{2}{3}\mu_{\mathrm{eff.}}\frac{\partial u_k}{\partial x_k}\delta_{ij}$
Mass transfer	$\frac{\partial}{\partial t}\left(\rho\omega_n\right) + \frac{\partial}{\partial x_i}\left(\rho u_i \omega_n\right) = \frac{\partial J_{jn}}{\partial x_j} + S_R$
Species model (Fick's law)	$J_{jn} = \left(\rho D_{\mathrm{m},n} + \frac{\mu_t}{\mathrm{Sc}_t}\right)\frac{\partial \omega_n}{\partial x_j} + \frac{D_{T,n}}{T}\frac{\partial T}{\partial x_j}$
Turbulence model (Realizable $k-\varepsilon$)	$\mu_t = \rho C_\mu \frac{k^2}{\varepsilon}$ $\frac{\partial}{\partial t}(\rho k) + \frac{\partial}{\partial x_j}\left(\rho k u_j\right) = \frac{\partial}{\partial x_j}\left[\left(\mu + \frac{\mu_t}{\sigma_k}\right)\frac{\partial k}{\partial x_j}\right] + G_k + G_b - \rho\varepsilon - Y_M$ $\frac{\partial}{\partial t}(\rho\varepsilon) + \frac{\partial}{\partial x_j}\left(\rho\varepsilon u_j\right) = \frac{\partial}{\partial x_j}\left[\left(\mu + \frac{\mu_t}{\sigma_\varepsilon}\right)\frac{\partial \varepsilon}{\partial x_j}\right] + \rho C_1 S\varepsilon - \rho C_2\frac{\varepsilon^2}{k+\sqrt{t\varepsilon}} + C_{1\varepsilon}\frac{\varepsilon}{k}C_{3\varepsilon}G_b$ $C_{1\varepsilon} = 1.44, C_2 = 1.9, C_1 = \max\left[0.43, \frac{\eta}{\eta+5}\right], \eta = S\frac{k}{\varepsilon}, S = \sqrt{2S_{ij}S_{ij}}, \delta_k = 1.0, \delta_\varepsilon = 1.2$
Momentum source (for porous media)	$f_i = -\left(\frac{\mu}{\alpha}u_i + \frac{1}{2}\beta\rho\lvert u\rvert u_i\right)$
Energy equations (for porous media)	$\frac{\partial}{\partial t}\left[\chi\rho_f E_f + (1-\chi)\rho_s E_s\right] + \frac{\partial}{\partial x_j}\left[u_i\left(\rho_f E_f + p\right)\right] =$ $\frac{\partial}{\partial x_j}\left[\lambda_{\mathrm{eff.}}\frac{\partial T}{\partial x_j} - \left(\sum_n h_n J_{jn}\right) + u_i\left(\tau_{ij}\right)_{\mathrm{eff.}}\right]$

reactor via the central nozzle and annular nozzle, respectively. Low-temperature water flows into the reactor via the TW inlets to protect the shell from high-temperature mainstream. The porous tube separates the TW region and reaction region. The pressure shell withstands the high pressure inside the reactor. The retaining rings support the structures. The detailed specifications of the reactor are presented in Table A.1 [10].

To numerically investigate the heat and mass transfer inside the TWR, a 2-D axisymmetric model (Fig. 2) was developed considering negligible variations in circumference. In Fig. 2, different flow regions are colored differently and interior boundaries are marked by thickened lines. All the outer walls were set with the thermally adiabatic boundary conditions (BC) since the reactor was covered by thermal insulation material during experiments. The reasons for highlighting the 'top region' and the 'below-nozzle region' will be discussed in Section 3. Additionally, all the five fluid inlets were modeled with prolonged channels to smooth out temperature gradients adjacent to the inlets. With this approach, unrealistic conductive heat loss from the computational domain could be avoided at the inlet boundaries (when compare with the open-inlet boundary conditions).

2.2. Numerical mesh

The numerical mesh structure is illustrated in Fig. 2. Triangle meshes are used for the TW region, the reaction region, and the solid region. Orthogonal meshes are used for the near-wall regions, the fluid channels (central jet, annular jet, and the outlet channel), and the porous media. It is noteworthy that the mesh of the porous media should be carefully designed to avoid divergence of the simulation in this case. As shown in Fig. 2(c), finer meshes (edge size at around 0.5 mm) are used in the upstream ($x < 0.375$ m) of the reaction region to capture sufficient flow details. In addition, the meshes near the nozzle are further refined (Fig. 2(a)). While for the TW region and downstream ($x > 0.375$ m) of the reaction region where velocities are small, coarser meshes with an edge size of around 2 mm are used. To improve the mesh quality at corners, some sharp corners are blunted (Fig. 2(b)).

To consider the turbulent effects in boundary layers, the wall function 'Enhanced Wall Treatment '(EWT) [32] was selected to model near-wall regions because it adapts to cases with small ($y^+ < 3$) or large ($y^+ > 30$) thickness of the first near-wall mesh. Here, y^+ is the dimensionless distance to the wall according to the logarithmic law of the wall. As for the mesh, quadrilateral inflation layers were adopted for the near-wall regions. For the near-wall regions near the nozzle (Fig. 2(a)), the wall-adjacent meshes were placed at $y^+ < 3$ to resolve viscous sub-layers. For the near-wall regions far from the nozzle (Fig. 2(d)), the wall-adjacent meshes were placed at fully-turbulent outer region ($y^+ > 30$) to save computational cost. During transient simulations, the y^+ values of the wall-adjacent meshes are changing before steady state. When the y^+ values of some wall-adjacent meshes sometimes fall in $3 < y^+ < 10$ (the buffer layer), other wall functions will perform ineffectively while the EWT will give a reasonable near-wall velocity profile [32]. Furthermore, the overall meshes are refined to pass the grid independence test, which are presented in Table A.2 and Fig. A.1.

2.3. Governing equations

Continuity and conservation equations were solved for momentum transport, heat transfer and mass transfer in the reactor. Fick's law was used to model the species transport and 'realizable $k-\varepsilon$ model' was adopted to model turbulence since it shows superior accuracy in round-jet simulations when compared with 'Standard $k-\varepsilon$ model [32]'. For the porous media, the pressure loss and heat and mass transfer within the porous media were considered. All governing equations are summarized in Table 1. Details on modeling of chemical reaction and thermal properties are presented below.

2.3.1. Chemical reaction model

The oxidation of methanol was modeled as a one-step reaction:

$$CH_3OH + 1.5O_2 \rightarrow CO_2 + 2H_2O. \quad (1)$$

Eddy Dissipation Model [33] (EDM) was adopted to simulate the interaction between the turbulence and chemical reactions in the reactor, which contributes to the source term S_R in the mass transfer equation. The EDM assumes that the reactions are very fast while the turbulence mixing is relatively slow. Thus, the reaction rate is limited by the turbulence mixing rate. With the EDM, Arrhenius reaction rates are not calculated while the reaction rates are estimated based on the turbulence field (k and ε).

2.3.2. Thermal properties

For each considered thermal property Φ, it is dependent on local temperature and pressure,

$$\Phi = \Phi(T, P). \tag{2}$$

In this study, the operating pressure of the reactor fluctuates between 22.5 MPa and 23.5 MPa, while the temperature is in the range between 300 K and 900 K. Therefore, the thermal properties of species vary more with the temperature variation than the pressure variation. Thus, we adopted the Low Mach Number Assumption [34,35], which assumes the thermal properties of species are functions of temperature at constant pressure ($P_0 = 23$ MPa) with negligible effects of pressure change. Hence, the thermal properties are determined as

$$\Phi = \Phi(T, P_0). \tag{3}$$

In this study, thermal properties (ρ, c_P, λ, and μ) of H_2O, CO_2, O_2, and CH_3OH was linearly interpolated based on NIST database [36], as shown in Fig. A.2. The interpolated thermal properties of H_2O, CO_2, and O_2 are in the range from 273 K to 1773 K, and those of CH_3OH are in the range from 273 K to 930 K. Such temperature ranges are sufficient to cover the temperature variations in the reactor.

2.4. Simulation settings

A commercial CFD software, Ansys Fluent, was used for the numerical simulations. The pressure-based solver with double precision was adopted. PISO scheme was applied for the pressure-velocity coupling. PRESTO! scheme, which suits problems with gravity effects, was adopted for the spatial discretization of the pressure term. Second Order Upwind scheme was selected for the discretization of momentum, energy, and species transport equations. First Order Implicit scheme was used for transient formulations. To alleviate numerical fluctuations due to buoyancy, a non-reactive case was simulated until steady-state and then the steady-state result was used as the initial condition of the consecutive transient reactive simulations. The boundary condition (BC) differences between the non-reactive case and the reactive case are only reflected by the species concentrations at the inlets. In the non-reactive case, pure water is injected into the reactor, while in the transient reactive case, the injections are methanol and oxygen. When the residuals of continuity and momentum equations are lower than 10^{-5}, the residual of energy equation is at the order of 10^{-9}, and the monitored velocity is stable, the simulation at present time step is considered to be converged. With this criteria, a time-step size of 0.01 s was adopted for the transient simulation to balance accuracy and computational cost. For the simulation time, a computer with a 6-core 3.2 GHz CPU takes around 2 weeks to finish a 70-second simulation case.

2.5. Validation

Experimental data was acquired from the pilot-scale reactor presented in our previous work [10]. In this study, temperature was measured along the central axis of the reactor by a ten-point thermal couple every 10 s. The ten-point thermal couple was inserted into the center of reactor and protected by a thin steel tube. The temperature of the outlet stream was measured by a separate thermal couple. To validate the numerical model with the experimental data, flow conditions (Table 2) of the validation case are consistent with those of the experiment. The comparison between the simulation results and the experimental data is shown in Fig. 3. In this comparison, the '0 s' is defined as the moment when the temperature at the central axis starts to rise due to the reaction. The curves from the simulation and the experiment have a qualitatively similar downward trend. In the flow direction, experimental data shows that significant temperature drops occur near two positions, i.e. $X = 0.4$ m and $X = 0.72$ m. Accordingly, for the simulation results, there are also two significant temperature drops at $X = 0.2$ m and $X = 0.6$ m, respectively. When analyzing with respect to time, for the experimental data, the peak temperature measured at the upstream of reactor rises from 623 K and stabilizes at around 860 K in 250 s. While for the simulation results, the peak temperature rises from 650 K and stabilizes at around 840 K in 70 s and the temperature varies at a very slow rate from 70 s to 200 s (temperature variations after 200 s are negligible).

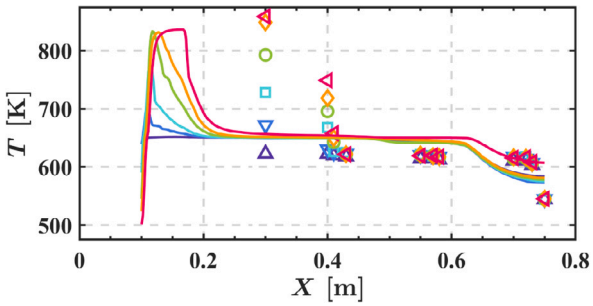

Fig. 3. Validation of numerical model with experiment by comparison of central-axis temperature. Lines represent simulation data at 0 s (—), 10 s (—), 20 s (—), 30 s (—), 70 s (—), and 200 s (—); symbols represent experimental data at 0 s (△), 50 s (▽), 100 s (□), 150 s (○), 200 s (◇), and 250 s (◁).

Although the simulation and experiment results are qualitatively similar, the quantitative deviations do exist. The errors of simulation may be attributed to the two sub-models for supercritical conditions, i.e. the chemical reaction model and the turbulence model. For the former, we adopted a one-step reaction mechanism between CH_3OH and O_2 because a multi-step reaction mechanism would be too computationally expensive and involve many uncertainties. Neglecting detailed reaction mechanism may lead to inaccurate predictions of the ignition time and the temperature of reaction products [37]. As for the turbulence model, the inaccuracy of current RANS models for supercritical cases has been reported in literature [38,39]. The inaccuracy of turbulence model may lead to the inaccurate flow fields and turbulence mixing rate. However, instead of pursuing a quantitative accurate simulation with high computational cost, this study aims at a qualitative analysis of the hydrothermal flame in supercritical conditions. Based on such a scope, the developed numerical model is sufficient to support this study.

3. Results and discussions

To investigate the hydrothermal flame formation, a simulation with intermediate operating conditions was conducted as a base case and the corresponding flow conditions are listed in Table 2. Using the base case as a reference, three series of simulations were designed to further investigate the formation of hydrothermal flame. As shown in Table 3, different simulation series have different feed temperatures (T_{AJI}, temperature at annular jet inlet), mass concentrations of CH_3OH in the feed jet (ω_{CH_3OH}), and widths of the annular jet inlet (W_{AJI}), while other variables (e.g. mass flow rates at inlets, ω_{O_2}, T_{CJI}, T_{TW1}, T_{TW2}, and T_{TW3}) were held consistent with the base case. Since conditions of the validation case (Table 2) are similar to the base case, the validation case is added into the following comparisons. In this section, we will analyze the base case first and then analyze the effects of different variables.

3.1. Analysis of base case

Video S1 (contained in the supplementary material) and Fig. 4 show the time-evolving development of the hydrothermal flame. From 3 s to 18 s, the reactor is at open-flame stage where the annular jet bends outwards from the central axis after leaving the nozzle. At this stage, a local hot spot appears at the corner of the annular jet and then becomes a small open flame. The heated fluid flows upwards along the outer

Table 2
Boundary conditions of inlets for validation case and base case (operating pressure is 23 MPa).

			AJI	CJI	TW1	TW2	TW3	Wall	Axis	Outlet
Base Case	ω	CH_3OH	0.06	0	0	0	0	Adiabatic Non-slip	Zero-flux	$P_{gauge} = 0$
		H_2O	0.94	0	1	1	1			
		O_2	0	1	0	0	0			
		T [K]	660	298.15	630	515	298.15			
		$\dot{m}$ [kg/s]	0.00292	0.00066	0.00455	0.00259	0.00469			
		Re	2188	3691	10636	3576	841			
Validation Case	ω	CH_3OH	0.04	0	0	0	0			
		H_2O	0.96	0	1	1	1			
		O_2	0	1	0	0	0			
		T [K]*	680	298.15	630	530	298.15			
		RSD_T **	0.1%		0.1%	0.8%				
		$\dot{m}$ [kg/s]*	0.00317	0.00057	0.00373	0.00237	0.00352			
		$RSD_{\dot{m}}$ **	8.0%	18.8%	1.8%	2.7%	3.3%			
		Re	2445	3168	8707	3474	631			

* Temperature and mass flow rate fluctuate during experiment, values adopted for boundary conditions are averaged over 250 s (interval of measurement is 10 s).
** RSD is relative standard deviation of measured values.

Table 3
Characteristic parameters of different simulation cases..

		T_{AJI} [K]	ω_{CH_3OH}	W_{AJI} [mm]	Re^*_{AJI}	OER**
Base case		660	6%	1	2188	2.5
Series 1	Case 1	635	6%	1	950	2.5
	Case 2	680	6%	1	2252	2.5
	Case 3	700	6%	1	2223	2.5
Series 2	Case A	660	4%	1	2188	3.8
	Case B	660	8%	1	2188	1.9
	Case C	660	10%	1	2188	1.5
Series 3	Case i	660	6%	2	2051	2.5
	Case ii	660	6%	3	1903	2.5
Validation case		680	4%	1	2445	3.0

* Reynold numbers are estimated by assuming $\omega_{CH_3OH} = 0$ and $\omega_{H_2O} = 1$.
** Oxygen excess ratio.

wall of the nozzle and leads to a significant temperature rise at the top region. From 18 s to 50 s, the reactor is at the transitional stage, where the outwards bending annular jet gradually stretches inwards and slightly merges with the central oxygen jet. In addition, the volume of flame increases and the temperature of the top region continues to increase while the upward heated flow becomes slower. The 50 s to 70 s is the closed-flame stage where the double concentric jets are combining and gradually stretching downwards. In addition, as the flame size, temperature, and velocity of the merged jet increase, the hot fluid no longer flows upwards into the top region. To further understand the phenomenon happening inside the TWR, the following discussions will specifically focus on the top region and below-nozzle region (defined in Fig. 2).

3.1.1. Top region

Fig. 5(a) shows the velocity profile near the nozzle wall at the top region. The profiles before 50 s and after 50 s are quite different. Before 50 s, X-velocity is negative which means the fluid flows upwards along the nozzle wall to the roof of the reactor. The reason for the upward flow is illustrated in Fig. 5(b), which shows the fluid temperature near the nozzle is much higher than those at the nozzle wall ($R = 0.125$ m) and other positions at the same cross-section. The high-temperature fluid has a lower density and hence flows upwards due to buoyancy. However, as the average temperature of the top region (T_{top}) grows and the average density (ρ_{top}) drops, at around 50 s, the hot fluid below the nozzle no longer flows upwards to the top region. At this stage, the T_{top} is far higher than the temperature at the nozzle wall (Fig. 5(b)). Hence, driven by buoyancy, the near-nozzle-wall fluid with a high density turns around and flow downwards along the cold nozzle wall. Thus, a positive X-velocity is observed after 50 s in Fig. 5(a).

3.1.2. Below-nozzle region

Three stages of the hydrothermal flame formation – the open-flame stage, transitional stage, and closed-flame stage – show interesting characteristics at the below-nozzle region. Fig. 6(a), 6(b) and 6(c) present typical distributions of the O_2 concentration, fluid density, reaction heat, and velocity fields at the three stages, respectively. We found that buoyancy plays an important role in the development of hydrothermal flame.

At the open-flame stage, the oxygen concentration difference between the two sides of the annular jet is noticeable. Here, the side closer to the central jet is defined as the inward side while the side further away from the central jet is defined as the outward side. The oxygen concentration at the inward side is over 60% while almost no oxygen is at the outward side (Fig. 6(a) left panel). Hence, as shown in the left panel of Fig. 6(c), strong reactions between CH_3OH and O_2 happen at the inward side of the annular jet, while almost no reaction happens at the outward side of the annular jet. The released reaction heat leads to a high temperature between the annular jet and central jet, which contributes to the formation of the hydrothermal flame. Thus, low density at the inward side of the annular jet is observed in Fig. 6(b) left panel. Due to the buoyancy, the low-density fluid tends to flow upwards and impedes the downward development of the annular jet. Overall, the strong buoyancy induced by the heated fluid and the comparably weak inertial force of the annular jet lead to the open flame.

At the transitional stage, the bending annular jet entrains oxygen from the inward side to the outward side (Fig. 6(a) middle panel). The entrainment enhances the reaction intensity at the outward side of the annular jet (Fig. 6(c) middle panel). The released reaction heat increases the temperature and fluid expansion at the outward side. It is the expanded low-density fluid gathering at the outward side (Fig. 6(b) middle panel) that helps the annular jet to stretch downwards. The hydrothermal flame gradually develops from an open flame into a closed flame in this stage.

At the closed-flame stage, the oxygen concentration at the outward side is still lower than that at the inward side(Fig. 6(a) right panel). The reactive area (Fig. 6(c) right panel) increases because of better mixing of the annular and central jets. However, the density (Fig. 6(b) right panel) on the both sides of the annular jet is comparable, indicating that the buoyancy acting on the annular jet is weakened. Overall, the weakened buoyancy acting on the annular jet and the comparably strong inertial force of the annular jet lead to the closed flame.

The average temperature over the radial direction from $R = 0$ m to $R = 0.125$ m (width of the below-nozzle region) are calculated to quantify the hydrothermal flame at the below-nozzle region. The radially averaged temperature distribution along the X axis is shown in Fig. 7(a). If the hydrothermal flame core is defined as the position where the max radial averaged temperature occurs, it is obvious that the temperature and X-coordinate of the hydrothermal flame core

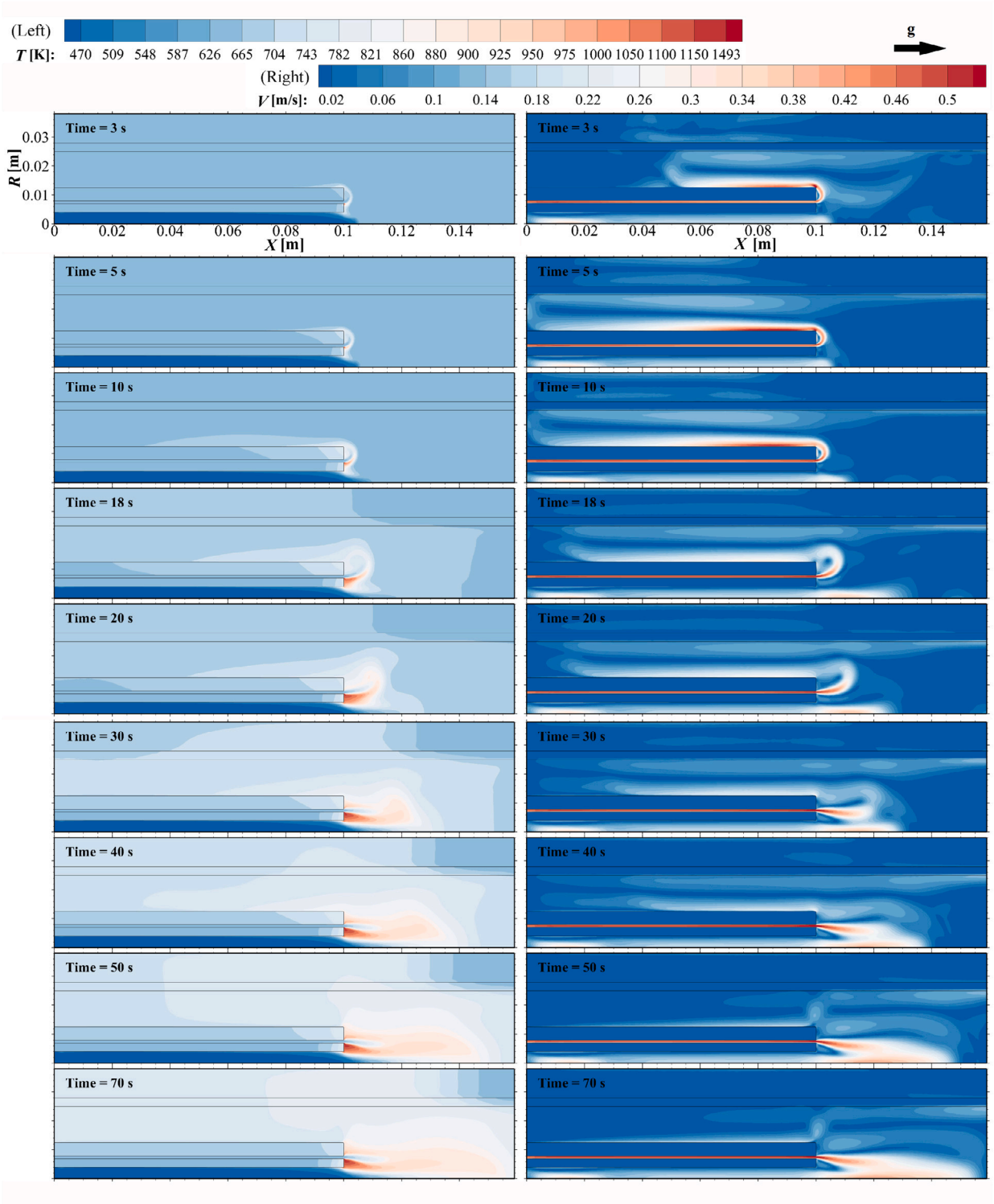

Fig. 4. Numerical results of base case: temperature and velocity fields at different time steps.

grow with time. And steep temperature gradients exist near the nozzle during the development of the hydrothermal flame. Furthermore, the hydrothermal flame imposes a great effect on the porous wall which is designed to protect the reactor. As shown in Fig. 7(b), after 30 s, a high local temperature occurs in the porous wall. As time goes on, the max temperature and temperature gradient continue to increase. Even though the temperature in the porous wall is much lower than that of the hydrothermal flame core, the resulted temperature gradient is a noticeable problem that will lead to thermal stresses and shorten the lifetime of the porous wall [8].

To reveal how the mixing of jets affect the temperature of the flame, the radially averaged temperature of the below-nozzle region at 70 s is shown in Fig. 8(a). Interestingly, there are two peaks of the radially averaged temperature along the axial direction. One is close to the nozzle (X = 0.1 m) while the other one is the global maximum (the hydrothermal flame core) located at X = 0.13 m. The velocity profiles at different positions (Figs. 8(b)–8(e)) show the development of concentric

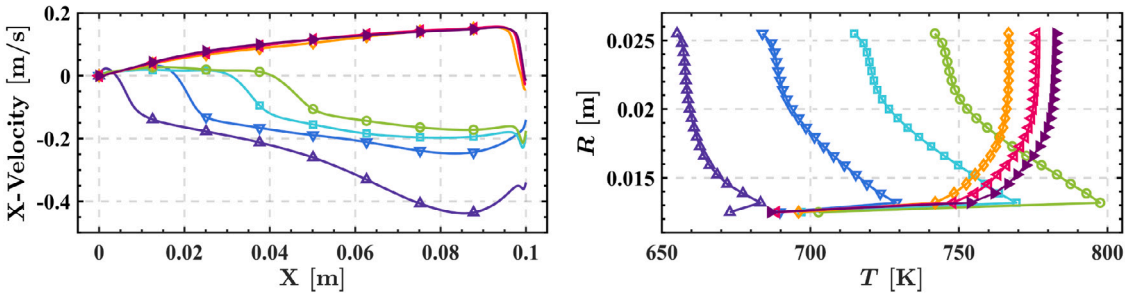

(a) Axial velocity profile near the nozzle wall. (b) Temperature profile at $X = 0.05$ m.

Fig. 5. Numerical results of base case: (a) velocity and (b) temperature profiles at top region. Symbols represent simulation data at 10 s (▲), 20 s (▼), 30 s (□), 40 s (○), 50 s (◆), 60 s (◀), and 70 s (▶).

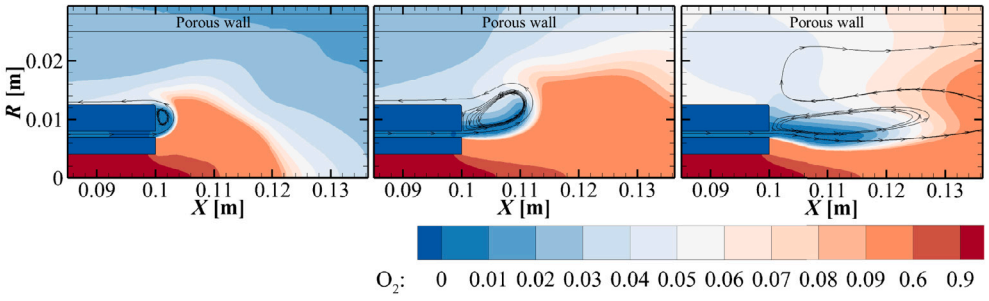

(a) Mass concentration field of oxygen.

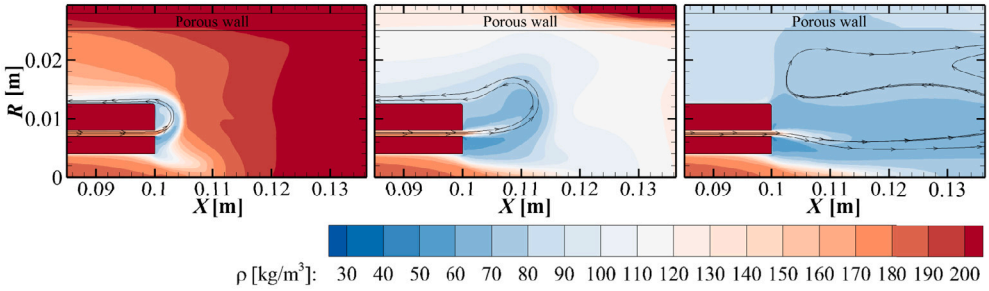

(b) Fluid density fields.

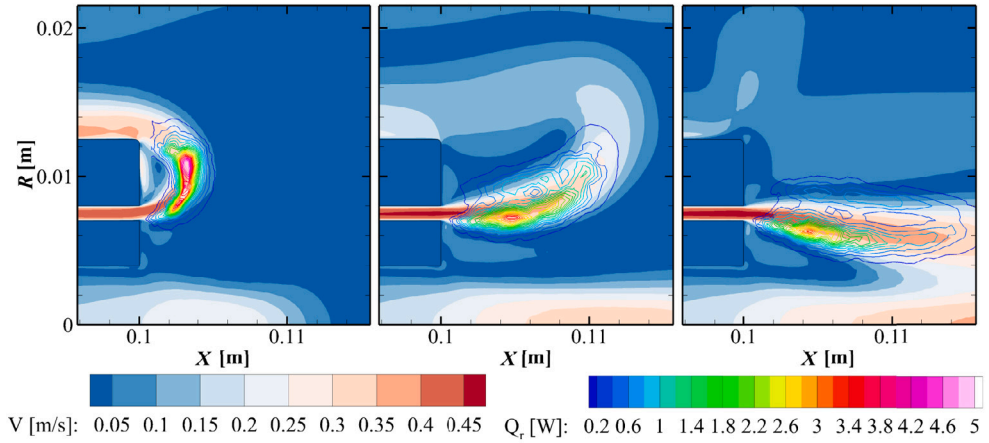

(c) Velocity fields with reaction heat.

Fig. 6. Numerical results of base case: flow fields near nozzle at open-flame stage at 10 s (left panel), transitional stage at 21 s (middle panel), and closed-flame stage at 70 s (right panel).

jets. For $X < 0.13$ m, the concentric jets are separated while for $X \geq 0.13$ m, the concentric jets merge into a combined jet due to the radial momentum diffusion. The combination or separation of two concentric jets has been illustrated by Chigier et al. [40]. Profiles at $X = 0.1005$ m (Fig. 8(b)) display the 'dead zones' where the velocity is low. Hot fluid accumulates in the 'dead zones' and leads to local hot spots at $X = 0.1005$ m due to weak convection and buoyancy. Additionally, max temperature occurs at $X = 0.13$ m (Fig. 8(d)) where the two concentric jets merge because of the good mixing of CH_3OH and O_2. As the velocity and concentrations of reactants decrease, the fluid temperature

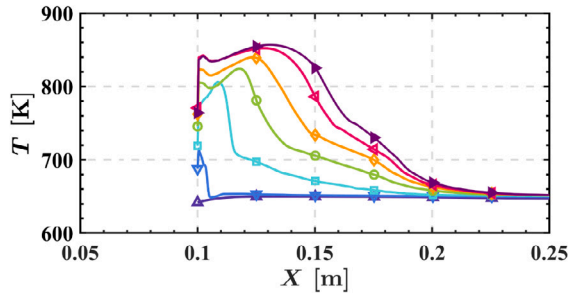

(a) Radially averaged (from $R = 0$ m to $R = 0.125$ m) temperature of below-jet region.

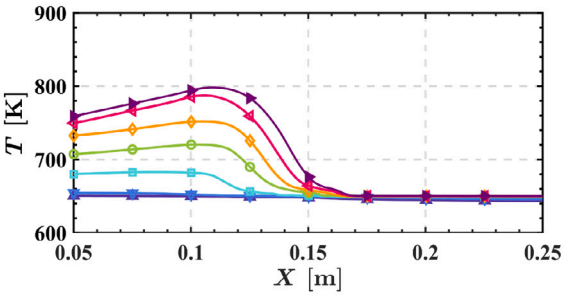

(b) Average temperature of porous wall.

Fig. 7. Numerical results of base case: temperature distribution in below-jet region and porous wall at 10 s (△), 20 s (▽), 30 s (□), 40 s (○), 50 s (◇), 60 s (◁), and 70 s (▷).

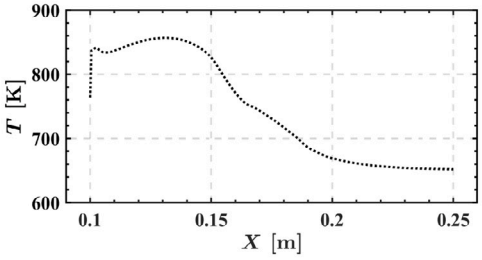

(a) Radially averaged (from $R = 0$ m to $R = 0.125$ m) temperature at 70 s.

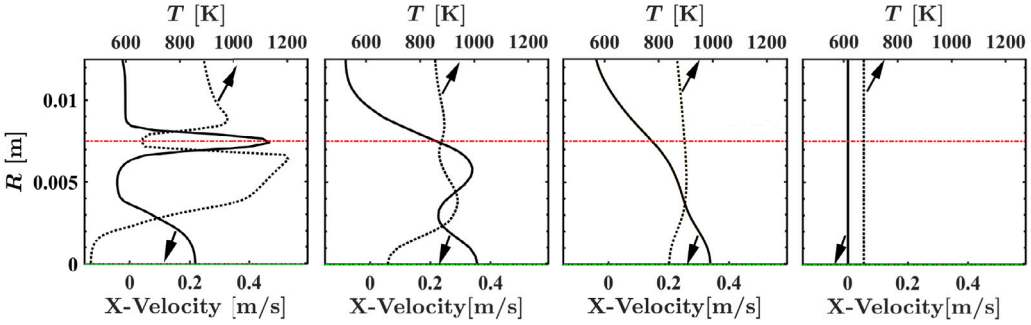

(b) $X = 0.1005$ m (c) $X = 0.115$ m (d) $X = 0.13$ m (e) $X = 0.2$ m

Fig. 8. Numerical results of base case: temperature profiles (▪▪▪▪) and velocity profiles (——) at 70 s. R-coordinate of the annual nozzle (▪ ▪ ▪) and central nozzle (▪ ▪ ▪) are marked.

decreases in the downstream. Our simulation shows that the core of hydrothermal flame occurs at the point where the fuel and oxygen are fully mixed when fluids are injected in the gravity direction. Hicks et al. [20]'s experiment also emphasized the importance of mixing by showing that the ignition of supercritical hydrothermal flame happens at the well-mixed point of fuel and oxygen when fluids are injected in the opposite direction of gravity.

3.2. Effects of different flow conditions

In addition to the base case, three series of simulations (Table 3) were conducted to analyze the effects of different flow conditions. Fig. 9 shows the quasi-steady flame shapes under various conditions. In this study, the quasi-steady state means when the radially average temperature at $X = 0.13$ m changes less then 0.1 K/s. After the quasi-steady state, increasing simulation time makes little difference to the flame structure. At the quasi-steady states of the base case, Case A, Case B, Case C, Case 2, Case 3 and the validation case, the flame develops to the closed-flame stage (see discussions in Section 3.1). However, the other cases cannot develop into closed flames and eventually stay at the open-flame stage. The flame shapes and flow conditions in Fig. 9 show that either low T_{AJI} or high W_{AJI} can lead to open flames at quasi-steady state.

When compared to closed flames, open flames may increase operational risks of the TWR. When holding ω_{CH_3OH} and T_{AJI} constant but increase the flow area of the annular nozzle, the closed flame (base case) will change to open flame (Case i and Case ii). The open flame conditions tend to result in higher local temperature and temperature gradient in the porous wall (Fig. 10(b)). The high temperature gradient may induce thermal stress that would potentially impair the porous wall. In addition, as shown in Fig. 10(c), the Case i and Case ii with open flames tend to take longer time (i.e. 250 s) to reach quasi-steady states in comparison to the base case which only takes 50 s. Thus, under the same flow conditions, the start-up of the open-flame cases would be slower than that of the closed-flame cases.

Apart from the W_{AJI}, Figs. 10(a), 10(b), and 10(c) also show the effects of ω_{CH_3OH} and T_{AJI}. By comparing the base case, Case A, Case B, and Case C, it can be noticed that the increase of ω_{CH_3OH} leads to the higher overall temperature and steeper temperature gradient in the reactor (Fig. 10(a)) and the porous wall (Fig. 10(b)). Since the temperature is highly sensitive to the ω_{CH_3OH}, the feed with high ω_{CH_3OH} may be unsafe for the TWR. Fig. 10(c) indicates that increasing

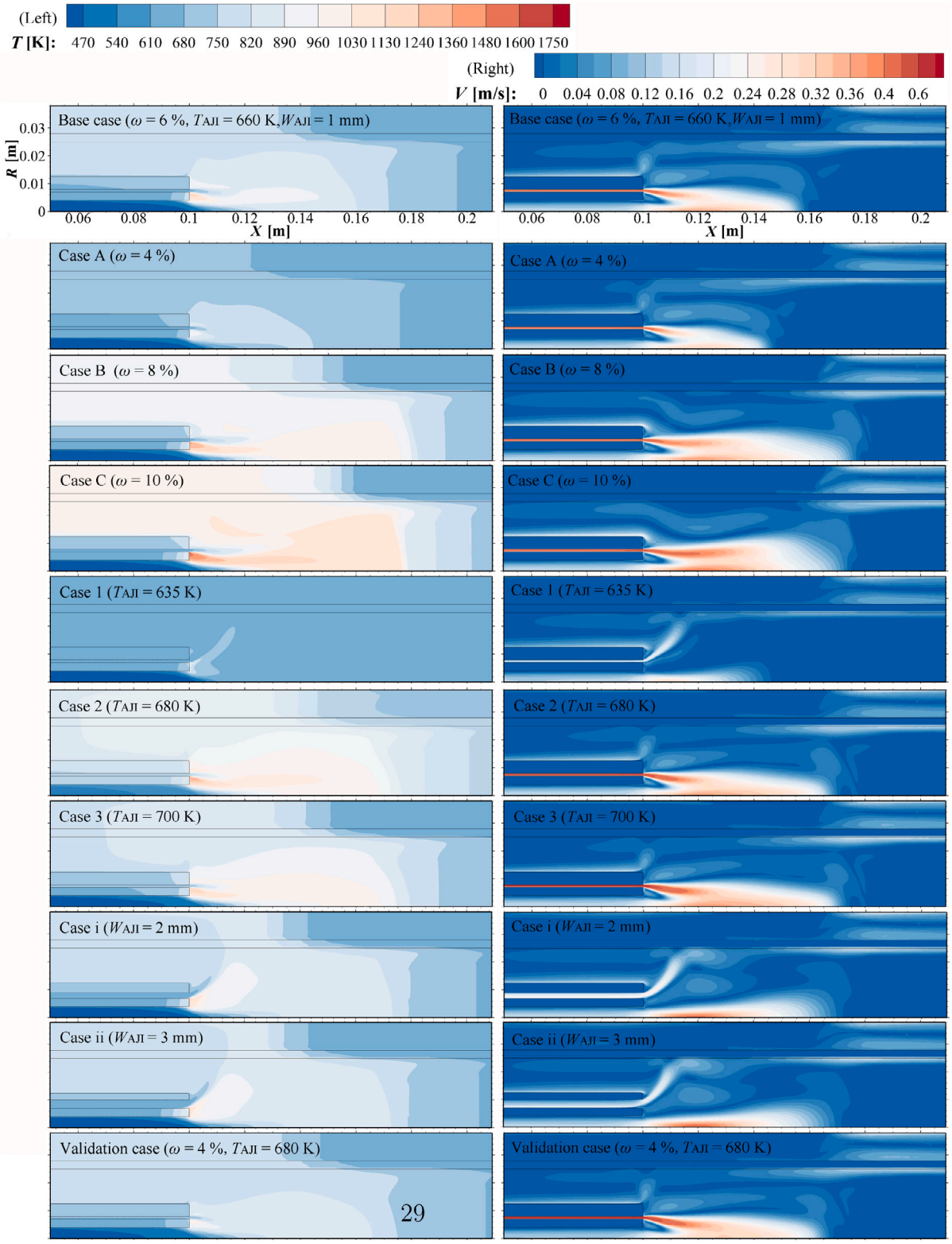

Fig. 9. Quasi-steady temperature and velocity fields of different cases.

ω_{CH_3OH} from 4% to 6% would accelerate the start-up process, while the further increase of ω_{CH_3OH} from 6% to 8% would significantly slow down the start-up process. Moreover, the spikes of Case A and Case B in Fig. 10(c) are caused by the transition from the open-flame stage to the closed-flame stage. For the base case with ω_{CH_3OH} = 6%, the transition occurs at around 30 s, while for Case B with ω_{CH_3OH} = 8% and Case C with ω_{CH_3OH} = 10%, the transition is delayed to 100 s and 120 s, respectively.

As for the effects of T_{AJI}, comparisons among the base case, Case 2, and Case 3 show that increasing feed temperature leads to an overall temperature increase and shorter time to reach quasi-steady state. While for the Case 1, the low T_{AJI} leads to open hydrothermal

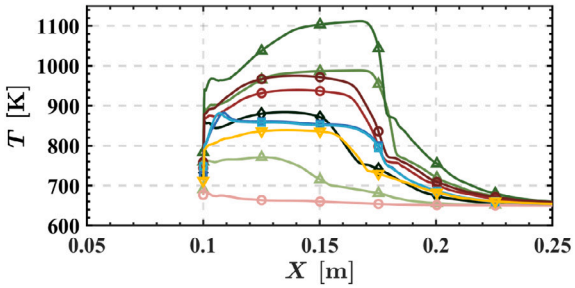

(a) Distributions of radially averaged (from $R = 0$ m to $R = 0.0125$ m) temperature.

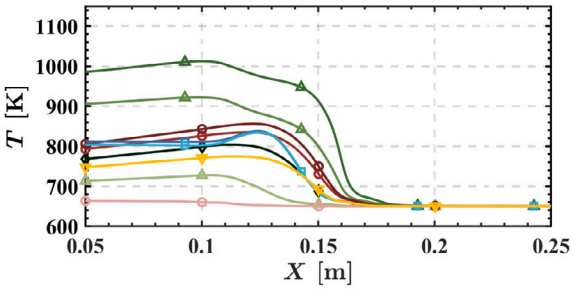

(b) Temperature distributions at porous wall.

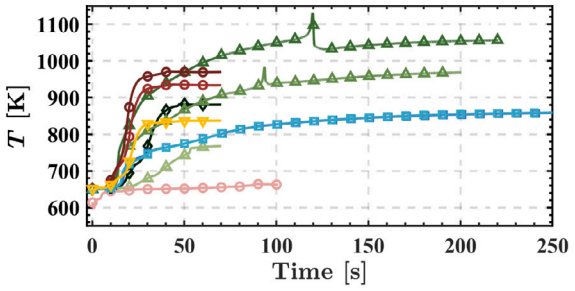

(c) Variations of radially averaged (from $R = 0$ m to $R = 0.0125$ m) temperature with time at $X = 0.13$ m).

Fig. 10. Comparisons among cases at quasi-steady state. Symbols represent different cases: base case (◆), Case A (△), Case B (△), Case C (△), Case 1 (○), Case 2 (○), Case 3 (○), Case i (□), Case ii (□), and validation case (▽).

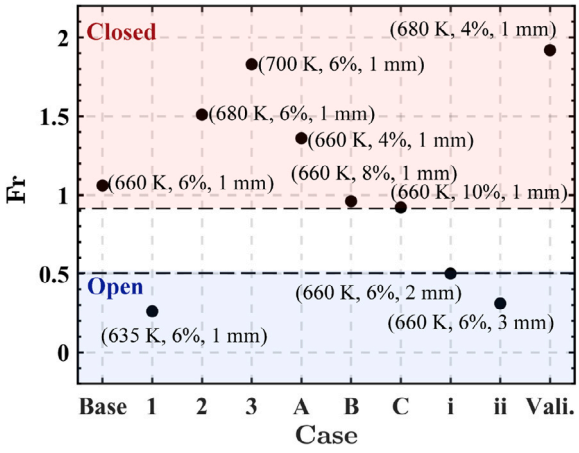

Fig. 11. Values of Fr for different cases with characteristic parameters ($T_{\mathrm{AJI}}, \omega_{\mathrm{CH_3OH}}, W_{\mathrm{AJI}}$).

flames. The T_{AJI} of Case 1 is 635 K which is lower than the critical temperature (650 K), which contributes to a relatively low temperature of the entire flow field. Although Case 1 imposes minimum threats on the reactor and the porous wall, the low temperature implies a weak reaction intensity, which compromises the oxidation efficiency.

The competition between the buoyant force and the inertial force, which plays an important role in the ignition [28] and evolution (Section 3.1.2) of hydrothermal flames, may explain the effects of $\omega_{\mathrm{CH_3OH}}$, T_{AJI}, and W_{AJI} on the shapes of hydrothermal flames. Firstly, increasing $\omega_{\mathrm{CH_3OH}}$ increases the buoyant force since the higher $\omega_{\mathrm{CH_3OH}}$ will release more reaction heat and result in a lower fluid density near the nozzle. And the increased buoyancy may delay the open-to-closed transition of the flame. Secondly, decreasing the feed temperature (T_{AJI}) reduces the inertial force of the jet and hence leads to the open flame. This is because the jet velocity is relative to the jet density when holding the mass flow rates constant at the inlets, and the density is highly sensitive to the temperature for trans-critical cases. For Case 1, the annular jet with sub-critical T_{AJI} has a high fluid density, a low velocity, and a low inertial force. Thirdly, increasing W_{AJI} is equivalent to increasing the flow area of nozzle that reduces the inertial force of the annular jet and hence leads to open flames.

3.3. Dimensionless analysis

Froude Number, Fr, is an effective dimensionless number to quantify 'negative buoyant jet' problems [41]. Reddy et al. [28] used the Fr to describe the effects of the inertial force and the buoyant force on the ignition delay of supercritical hydrothermal flames. In this section, the Froude Number is developed to be a criterion for predicting the shapes of hydrothermal flames. Such a dimensionless analysis will quantitatively guide the design of the operating conditions to avoid open flames inside the TWR.

As expressed in Eq. (4), Fr represents the ratio of the inertial force of the annular jet to the buoyant force of the low-density reacted fluid (the fluid heated by oxidation reactions),

$$\mathrm{Fr} = u_{\mathrm{AJI}} \sqrt{\frac{\rho_{\mathrm{AJI}}}{2L\left(\rho_{\mathrm{AJI}} - \rho_R\right) g}}, \tag{4}$$

where the subscript AJI denotes parameters of the feed at the annular jet inlet, L denotes the characteristic length, which is the radius of the porous tube in this case, and ρ_R is the density of the reacted fluid.

Fr of each case is calculated based on the boundary conditions (Tables 2 and 3) with the following assumptions.

- A constant pressure of 23 MPa is assumed in the reactor when calculating the thermal properties of fluids.
- Since the mass faction of H_2O is consistently over 80% before and after reactions for all cases, the mass fraction of H_2O is assumed to be 100% for simplified calculations.

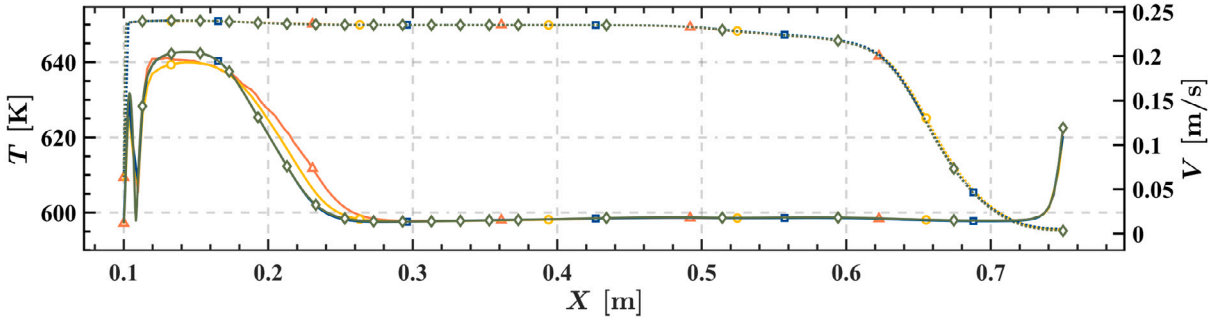

Fig. A.1. Grid independence test. Solid lines represent velocities and the dotted lines represent temperatures; symbols represent different meshes: Mesh 1 (△), Mesh 2 (○), Mesh 3 (□), and Mesh 4 (◇). .

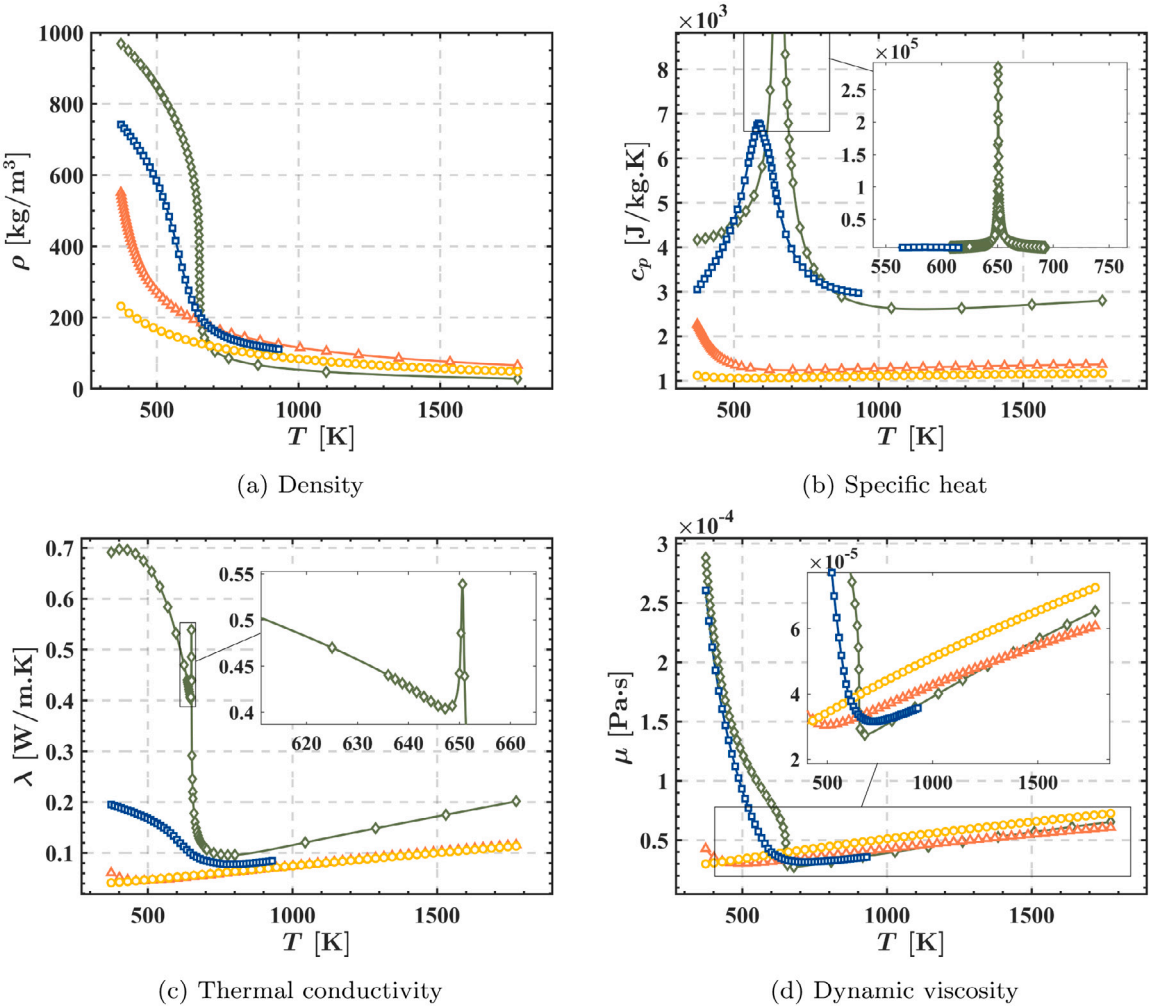

Fig. A.2. Piecewise linear interpolation of thermal properties of considered species. Lines represent properties from NIST dataset; symbols represent selected data points of CO_2 (△), O_2 (○), CH_3OH (□), and H_2O (◇).

- Since the temperature rise due to reaction only occurs at a narrow region near the nozzles, only the mass flow rates of the annular nozzle and the central nozzle are considered (mass flow rates of TW are excluded) when calculating Fr.

With the assumptions mentioned above and the two-property rule, the ρ_{AJI} in Eq. (4) can be determined by a given T_{AJI} and the constant pressure (23 MPa). Similarly, the $\rho_{\mathcal{R}}$ can be determined by the pressure and the enthalpy of the hot reacted fluid, $h_{\mathcal{R}}$, which can be calculated as,

$$h_{\mathcal{R}} = \frac{\dot{m}_{AJI}\left(h_{AJI} + \omega_{CH_3OH} \cdot \dot{m}_{AJI} \cdot \Delta h_c^0\right)}{\dot{m}_{noz}}, \tag{5}$$

where Δh_c^0 is the heat of combustion of CH_3OH, $\dot{m}_{noz}$ is the net mass flow rate of the annular and central nozzles, and h_{AJI} is the enthalpy of the feed determined by the given temperature, pressure, and species compositions at the annular nozzle inlet. The u_{AJI} in Eq. (4) can be

Table A.1
Specifications of TWR [10].

Parameter	Value
Reactor geometry	
Material	steel 321
Diameter and thickness of reactor vessel [mm]	$\phi 114 \times 17$
Effective length of reactor [mm]	760
Diameter and thickness of reactor outlet [mm]	$\phi 25 \times 4.5$
The porous tube geometry	
Material	steel 316 L
Diameter and thickness of porous tube [mm]	$\phi 60 \times 2.5$
Length [mm]	750
Porosity [%]	42.7
Viscosity coefficient [m^2]	6.2×10^{-12}
Inertia coefficient [m]	3.2×10^{-8}
Nozzle geometry	
Diameter and thickness of inner tube [mm]	$\phi 14 \times 3$
Length of inner tube [mm]	100
Diameter and thickness of outer tube [mm]	$\phi 25 \times 4.5$
Length of outer tube [mm]	100
Injection tube for transpiring water	
Diameter and thickness of injection tubes [mm]	$\phi 14 \times 3$
Position for TW1	H = 0.170 m,angle= 0°
Position for TW2	H = 0.435 m,angle= 120°
Position for TW3	H = 0.625 m,angle= 240°

* In this table, H is the distance to the top of the reactor.

Table A.2
Mesh size for grid independence test (Mesh 3 is adopted for this study).

	Edge size of grid [mm]		Number of elements
	Upstream (X < 375 mm)	Downstream (X > 375 mm)	
Mesh 1	2	2	45000
Mesh 2	1	1	77000
Mesh 3	0.5	2	139000
Mesh 4	0.2	0.5	454000

calculated as,

$$u_{AJI} = \frac{\dot{m}_{AJI}}{\rho_{AJI} A_{AJI}}, \quad (6)$$

where, A_{AJI} is the flow area of the annular jet.

The Fr of each case is listed in Fig. 11. For cases with Fr lower than 0.5, the buoyant force of the hot fluid outweighs the inertia force of the annular jet, so the hydrothermal flame is open. For cases with Fr larger than 0.9, the inertia force of annular jet outweighs the buoyant force of hot fluid, so the hydrothermal flame is closed. It should be noted that the threshold values of Fr given in this study is not general for real situations but specific to the current numerical model. Although we cannot give an exact threshold value of Fr as a universal criterion to predict the flame shape, the effectiveness of the Fr-based criterion has been demonstrated.

4. Conclusions

To provide insights of the fundamentals of the evolution and characteristics of hydrothermal flame, a 2-D transient numerical analysis on a supercritical water oxidation reactor with a transpiring wall was performed. The key conclusions are summarized as follow.

- At the beginning of reactions, upward flow occurs at the nozzle wall since the hot fluid out of the nozzle is driven to the top region by buoyancy. As time goes by, the temperature of the top region becomes much higher than the nozzle wall, then downward flow occurs at the nozzle wall due to gravity.
- In the below-nozzle region, the evolution of the hydrothermal flame is divided into three stages: open-flame stage, transitional stage, and closed-flame stage. The competition between the inertial force of the jet flow and the buoyant force of the hot fluids after absorbing reaction heat plays a critical role during the evolution of the hydrothermal flame.
- The core of the hydrothermal flame appears at the place where the two concentric jets are fully combined and mixed.
- By adjusting the feed temperature (T_{AJI}), the feed concentration (ω_{CH_3OH}), and the flow area of the annular jet inlet (W_{AJI}), two shapes of quasi-steady flame – the closed flame and the open flame – are found. Compared to the closed flame, the open flame may slow down the start-up process and increase operational risk due to hot spots in the porous wall. Thus, open flames should be avoided in real-life applications.
- The fluid temperature inside the reactor is highly sensitive to the feed concentration (ω_{CH_3OH}). A high concentration of feed may put the reactor at risk due to the high local temperature and steep temperature gradient. A high concentration of feed may also delay the transition from open-flame stage to closed-flame stage.
- The subcritical feed temperature (T_{AJI}) may result in an open flame at quasi-steady state. When the feed temperature is above the supercritical point, increasing the feed temperature leads to a higher overall temperature and faster start-up of the reactor.
- The Froude Number, Fr (Eq. (4)), which compares the importance of the inertial force and the buoyant force, is used to explain the causes of the different shapes of quasi-steady flame at different flow conditions. Dimensionless analysis shows that the open flame occurs when Fr is low (the buoyant force outweighs the inertial force). On the contrary, the closed flame occurs when Fr is high (the inertial force outweighs the buoyant force). Moreover, increasing feed concentration delays the open-to-closed transition of flame because the increased reaction heat augments the buoyant force of hot fluid. Similarly, decreasing feed temperature or increasing flow area of the annular jet inlet leads to open flames due to the decreased inertial force of the jet.

Looking forward, we have identified a couple of improvements of the current work that shall be explored in future studies. Firstly, a more advanced turbulence model could be explored to improve the accuracy of modeling supercritical fluids. Secondly, computational effective multi-step chemical mechanisms could be adopted to give more accurate reaction rates. Thirdly, the effects of TW, which is not considered in the dimensionless analysis of this study, could be further investigated. Actually, according to [4,30], the mass flow rate and temperature of the TW affect the thickness of the cold water film near the porous wall, which may slightly change the characteristic radius (the L in Eq. (4)) of the porous tube. Such an effect could be considered in a more generic dimensionless number in future works.

Declaration of competing interest

Fengming Zhang reports financial support was provided by National Natural Science Foundation of China. Fengming Zhang reports financial support was provided by Youth Innovation Promotion Association CAS. Fengming Zhang reports financial support was provided by Guangdong Basic and Applied Basic Research Foundation. Fengming Zhang reports financial support was provided by Guangzhou Science and Technology Projects. Fengming Zhang reports financial support was provided by Nansha District Science and technology project.

Data availability

No data was used for the research described in the article.

Acknowledgments

This work is partially supported by National Natural Science Foundation, China (NO. 51706049), Youth Innovation Promotion Association CAS, China (NO. 2017412), Guangdong Basic and Applied Basic Research Foundation, China (NO. 2021A1515010489), Guangzhou Science and Technology Projects, China (NO. 202102080627), and Nansha District Science and technology project, China (NO. 2021ms016), China.

Appendix A

Four cases with different upstream and downstream mesh sizes (Table A.2) were designed for the grid independence test. The grid independence test was conducted without gravity effects for fast convergence to save computational cost. Fig. A.1 shows the result of the grid independence test with temperature and velocity variations along the central axis of the four cases. To balance accuracy and computational cost, Mesh 3 (0.5 mm & 2 mm) was adopted for this study.

Appendix B. Supplementary data

Supplementary material related to this article can be found online at https://doi.org/10.1016/j.supflu.2022.105692.

References

[1] B. Xu, Y. Zhu, H. Jin, Y. Guo, J. Fan, Transcritical transition of the fluid around the interface, Phys. Fluids 33 (12) (2021) 122106, http://dx.doi.org/10.1063/5.0067825.
[2] N. Wei, D. Xu, B. Hao, S. Guo, Y. Guo, S. Wang, Chemical reactions of organic compounds in supercritical water gasification and oxidation, Water Res. 190 (2021) 116634, http://dx.doi.org/10.1016/j.watres.2020.116634.
[3] X. Du, R. Zhang, Z. Gan, J. Bi, Treatment of high strength coking wastewater by supercritical water oxidation, Fuel 104 (2013) 77–82, http://dx.doi.org/10.1016/j.fuel.2010.09.018.
[4] F. Zhang, J. Yang, J. Ma, C. Su, C. Ma, Optimization of structural parameters of an inner preheating transpiring-wall SCWO reactor, Chem. Eng. Res. Des. 141 (2019) 372–387, http://dx.doi.org/10.1016/j.cherd.2018.11.015.
[5] D. Xu, S. Wang, C. Huang, X. Tang, Y. Guo, Transpiring wall reactor in supercritical water oxidation, Chem. Eng. Res. Des. 92 (11) (2014) 2626–2639, http://dx.doi.org/10.1016/j.cherd.2014.02.028.
[6] F. Zhang, Y. Li, C. Jia, B. Shen, Effect of evaporation on the energy conversion of a supercritical water oxidation system containing a hydrothermal flame, Energy 226 (2021) 120406, http://dx.doi.org/10.1016/j.energy.2021.120406.
[7] B. Wellig, K. Lieball, P.R. von Rohr, Operating characteristics of a transpiring-wall SCWO reactor with a hydrothermal flame as internal heat source, J. Supercrit. Fluids 34 (1) (2005) 35–50, http://dx.doi.org/10.1016/j.supflu.2004.07.003.
[8] F. Zhang, C. Xu, Y. Zhang, S. Chen, G. Chen, C. Ma, Experimental study on the operating characteristics of an inner preheating transpiring wall reactor for supercritical water oxidation: Temperature profiles and product properties, Energy 66 (2014) 577–587, http://dx.doi.org/10.1016/j.energy.2014.02.003.
[9] C. Augustine, J.W. Tester, Hydrothermal flames: From phenomenological experimental demonstrations to quantitative understanding, J. Supercrit. Fluids 47 (3) (2009) 415–430, http://dx.doi.org/10.1016/j.supflu.2008.10.003.
[10] F. Zhang, J. Ma, C. Su, Study on the uniformity of water film in a transpiring wall reactor for supercritical water oxidation, Can. J. Chem. Eng. 98 (7) (2020) 1631–1644, http://dx.doi.org/10.1002/cjce.23726.
[11] P. Stathopoulos, K. Ninck, P.R. von Rohr, Hot-wire ignition of ethanol–oxygen hydrothermal flames, Combust. Flame 160 (11) (2013) 2386–2395, http://dx.doi.org/10.1016/j.combustflame.2013.05.006.
[12] T. Meier, M.J. Schuler, P. Stathopoulos, B. Kramer, P. Rudolf von Rohr, Hot surface ignition and monitoring of an internal oxygen–ethanol hydrothermal flame at 260 bar, J. Supercrit. Fluids 130 (2017) 230–238, http://dx.doi.org/10.1016/j.supflu.2016.09.015.
[13] J. Zhang, P. Li, J. Lu, X. Zheng, L. Wu, H. Nan, Supercritical hydrothermal combustion of nitrogen-containing compounds in a tubular reactor, Fuel 275 (2020) 117889, http://dx.doi.org/10.1016/j.fuel.2020.117889.
[14] B. Wellig, M. Weber, K. Lieball, K. Prikopsky, P.R. von Rohr, Hydrothermal methanol diffusion flame as internal heat source in a SCWO reactor, J. Supercrit. Fluids 49 (1) (2009) 59–70, http://dx.doi.org/10.1016/j.supflu.2008.11.021.
[15] M.D. Bermejo, C. Jimenez, P. Cabeza, A. Matias-Gago, M.J. Cocero, Experimental study of hydrothermal flames formation using a tubular injector in a refrigerated reaction chamber. influence of the operational and geometrical parameters, J. Supercrit. Fluids 59 (2011) 140–148, http://dx.doi.org/10.1016/j.supflu.2011.08.009.
[16] F. Zhang, Y. Zhang, C. Xu, S. Chen, G. Chen, C. Ma, Experimental study on the ignition and extinction characteristics of the hydrothermal flame, Chem. Eng. Technol. 38 (11) (2015) 2054–2066, http://dx.doi.org/10.1002/ceat.201300571.
[17] P. Cabeza, M.D. Bermejo, C. Jiménez, M.J. Cocero, Experimental study of the supercritical water oxidation of recalcitrant compounds under hydrothermal flames using tubular reactors, Water Res. 45 (8) (2011) 2485–2495, http://dx.doi.org/10.1016/j.watres.2011.01.029.
[18] R.M. Serikawa, T. Usui, T. Nishimura, H. Sato, S. Hamada, H. Sekino, Hydrothermal flames in supercritical water oxidation: investigation in a pilot scale continuous reactor, Fuel 81 (9) (2002) 1147–1159, http://dx.doi.org/10.1016/s0016-2361(02)00015-7.
[19] A. Sobhy, I.S. Butler, J.A. Kozinski, Selected profiles of high-pressure methanol-air flames in supercritical water, Proc. Combust. Inst. 31 (2007) 3369–3376, http://dx.doi.org/10.1016/j.proci.2006.07.253.
[20] M.C. Hicks, U.G. Hegde, J.J. Kojima, Hydrothermal ethanol flames in co-flow jets, J. Supercrit. Fluids 145 (2019) 192–200, http://dx.doi.org/10.1016/j.supflu.2018.12.010.
[21] R. Mari, B. Cuenot, J.-P. Rocchi, L. Selle, F. Duchaine, Effect of pressure on hydrogen/oxygen coupled flame–wall interaction, Combust. Flame 168 (2016) 409–419, http://dx.doi.org/10.1016/j.combustflame.2016.01.004.
[22] H. Huo, X. Wang, V. Yang, A general study of counterflow diffusion flames at subcritical and supercritical conditions: Oxygen/hydrogen mixtures, Combust. Flame 161 (12) (2014) 3040–3050, http://dx.doi.org/10.1016/j.combustflame.2014.06.005.
[23] X. Wang, H. Huo, U. Unnikrishnan, V. Yang, A systematic approach to high-fidelity modeling and efficient simulation of supercritical fluid mixing and combustion, Combust. Flame 195 (2018) 203–215, http://dx.doi.org/10.1016/j.combustflame.2018.04.030.
[24] M. Ren, S. Wang, J. Zhang, Y. Guo, D. Xu, Y. Wang, Characteristics of methanol hydrothermal combustion: Detailed chemical kinetics coupled with simple flow modeling study, Ind. Eng. Chem. Res. 56 (18) (2017) 5469–5478, http://dx.doi.org/10.1021/acs.iecr.7b00886.
[25] M. Ren, S. Wang, D. Roekaerts, Numerical study of the counterflow diffusion flames of methanol hydrothermal combustion: The real-fluid effects and flamelet analysis, J. Supercrit. Fluids 152 (2019) 104552, http://dx.doi.org/10.1016/j.supflu.2019.104552.
[26] C. Song, K. Luo, T. Jin, H. Wang, J. Fan, Direct numerical simulation on auto-ignition characteristics of turbulent supercritical hydrothermal flames, Combust. Flame 200 (2019) 354–364, http://dx.doi.org/10.1016/j.combustflame.2018.12.002.
[27] C. Song, T. Jin, H. Wang, Z. Gao, K. Luo, J. Fan, High-fidelity numerical analysis of non-premixed hydrothermal flames: Flame structure and stabilization mechanism, Fuel 259 (2020) 116162, http://dx.doi.org/10.1016/j.fuel.2019.116162.
[28] S.N. Reddy, S. Nanda, P. Kumar, M.C. Hicks, U.G. Hegde, J.A. Kozinski, Impacts of oxidant characteristics on the ignition of n-propanol-air hydrothermal flames in supercritical water, Combust. Flame 203 (2019) 46–55, http://dx.doi.org/10.1016/j.combustflame.2019.02.004.
[29] F. Zhang, C. Su, Z. Chen, J. Chen, Experimental study on the mixing characteristics inside an inner preheating transpiring-wall reactor for supercritical water oxidation, J. Supercrit. Fluids 156 (2020) http://dx.doi.org/10.1016/j.supflu.2019.104682.
[30] F. Zhang, C. Ma, CFD simulation of a transpiring-wall SCWO reactor: Formation and optimization of the water film, AIChE J. 62 (1) (2016) 195–206, http://dx.doi.org/10.1002/aic.15021.
[31] P. Feng, Y. Wang, D. Xu, W. Yang, G. Jiang, Effect of operating parameters on water film properties of transpiring wall reactor, J. Supercrit. Fluids 176 (2021) 105304, http://dx.doi.org/10.1016/j.supflu.2021.105304.
[32] ANSYS fluent theory guide, release r18.1, 2017, URL http://www.ansys.com.
[33] B. Magnussen, On the structure of turbulence and a generalized eddy dissipation concept for chemical reaction in turbulent flow, in: 19th Aerospace Sciences Meeting, 1981, p. 42, http://dx.doi.org/10.2514/6.1981-42.
[34] J. Liu, Y. Jin, P. Zhao, Z. Ge, Y. Li, Y. Wan, Analysis of heat transfer of supercritical water by direct numerical simulation of heated upward pipe flows, Int. J. Therm. Sci. 138 (2019) 206–218, http://dx.doi.org/10.1016/j.ijthermalsci.2018.12.028.
[35] A.L. Purohit, J.A. Misquith, B.R. Pinkard, S.J. Moore, J.C. Kramlich, P.G. Reinhall, I.V. Novosselov, Design of a small-scale supercritical water oxidation reactor. part II: Numerical modeling, Ind. Eng. Chem. Res. 60 (30) (2021) 11458–11469, http://dx.doi.org/10.1021/acs.iecr.1c00932.
[36] NIST, Thermophysical properties of fluid systems, 2021, URL https://webbook.nist.gov/chemistry/fluid/.
[37] A. Frassoldati, G. D'Errico, T. Lucchini, A. Stagni, A. Cuoci, T. Faravelli, A. Onorati, E. Ranzi, Reduced kinetic mechanisms of diesel fuel surrogate for engine CFD simulations, Combust. Flame 162 (10) (2015) 3991–4007, http://dx.doi.org/10.1016/j.combustflame.2015.07.039.

[38] F. Sun, Y. Li, O. Manca, G. Xie, An evaluation on the laminar effect of buoyancy-driven supercritical hydrocarbon fuel flow and heat transfer characteristics, Int. J. Heat Mass Transfer 142 (2019) 118414, http://dx.doi.org/10.1016/j.ijheatmasstransfer.2019.07.064.

[39] B. Liu, Y. Zhu, J.-J. Yan, Y. Lei, B. Zhang, P.-X. Jiang, Experimental investigation of convection heat transfer of n-decane at supercritical pressures in small vertical tubes, Int. J. Heat Mass Transfer 91 (2015) 734–746, http://dx.doi.org/10.1016/j.ijheatmasstransfer.2015.07.006.

[40] N. Chigier, J. Beér, The flow region near the nozzle in double concentric jets, 1964, http://dx.doi.org/10.1115/1.3655957.

[41] K.M. Talluru, S. Armfield, N. Williamson, M. Kirkpatrick, L. Milton-McGurk, Turbulence structure of neutral and negatively buoyant jets, J. Fluid Mech. 909 (2021) http://dx.doi.org/10.1017/jfm.2020.921.